Chapter 6

CFD based Investigation of Condensation of R-744 Inside an Ejector

In this chapter, we perform three dimensional simulations of the phase change process of R-744 inside an ejector geometry using Ansys CFX. We use two different phase change solvers available in Ansys CFX, namely, the equilibrium phase change solver and the droplet based non-equilibrium phase change solver. The real gas properties of R-744 are based on the Soave-Redlich-Kwong equation of state already built-in Ansys CFX and the Span-Wagner equation of state available in NIST REFPROP. Results related to the distribution of liquid mass fraction, droplet nucleation rate, droplet diameter etc. are presented and discussed.

6.1 Ejector computational domain, Mesh generation and Solver set-up details

Here we provide details on the ejector geometry, mesh generation and the various solver options
6.1) shows the cross-sectional view of the ejector along with
the various dimensions exposed by a plane passing through the axis and the suction inlet. The
geometry of the ejector and the block structured mesh are generated using the open source
133]. The mesh from GMSH needs to be converted to Ansys Fluent
format before it can be read in Ansys CFX. This is done with the help of utilities in the open
135] which can convert the mesh files from GMSH to Ansys

Fluent format. These Fluent format mesh files can be read in Ansys CFX. The block structured

6.2

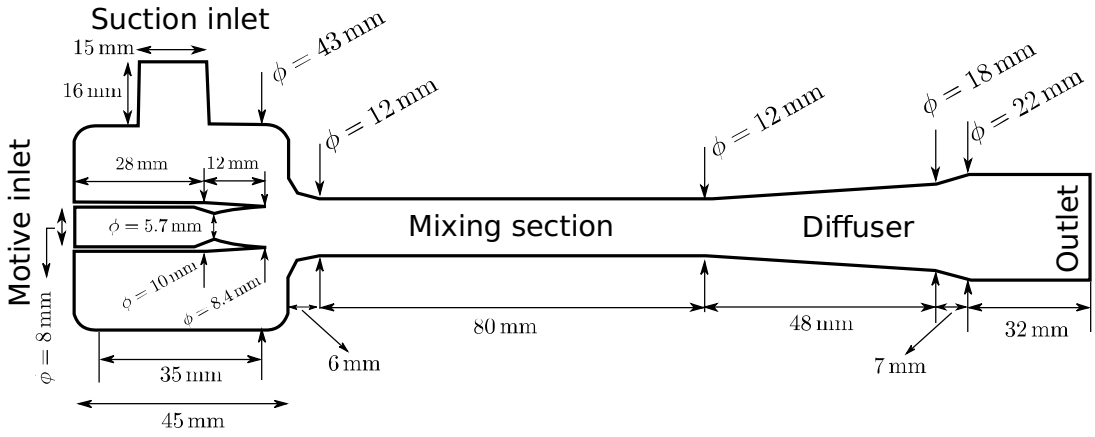

FIGURE 6.1: The cross-sectional view of the ejector exposed by a plane passing through its axis is shown here along with the main dimensions.

A total of 678979 hexahedral cells are used in the mesh with smaller mesh elements distributed near the center line of the ejector inside the motive nozzle, the mixing and the diffuser sections. A coarse mesh is used near the ejector walls (the non-dimensional wall distance $y^+ \gg 1$) in order to reduce the computational effort. Such an approach is justified since we are interested more in the phase change process in the bulk of the domain and not in accurately predicting the drag and heat transfer coefficients at the ejector walls. This necessitates the use of wall functions for the various physical quantities related to flow turbulence which are provided by the $k - \Omega$ SST model used in the current work.

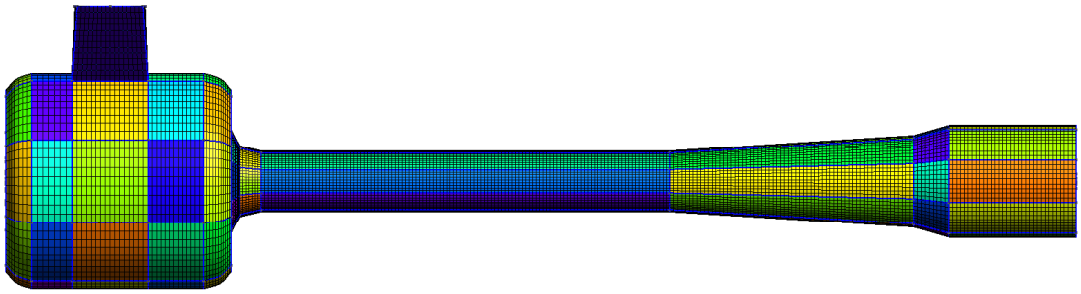

FIGURE 6.2: The block structured mesh generated inside the ejector geometry is shown here. 133] is used for the structured mesh generation. A total of 678979 hexahedral mesh elements constitute the mesh.

The various solver options with respect to spatial, temporal discretization and the phase change B.2 B.3 6.1 shows the various boundary and initial conditions for the main physical quantities used in the current work. A pressure equal to 80 bar and temperature equal to 315 K is specified at the inlet of the motive nozzle while the value of these quantities at the suction nozzle is 25 bar and 273.15 K respectively.

TABLE 6.1: Boundary and initial conditions used in the current work

Variable	Motive inlet	Suction inlet	Outlet	I.C.
Pressure	80 bar	25 bar	35 bar	55 bar
Temperature	315 K	273.15 K	Outflow	315 K
Vapor fraction	1	1	Outflow	1
Droplet number	0 m^{-3}	0 m^{-3}	Outflow	0
Turbulence intensity	5%	Zero gradient	Outflow	5%

A pressure equal to 35 bar is specified at the outlet of the ejector while 'outflow' condition is used for temperature. The volume fraction of the vapor phase at the motive and the suction inlets is equal to one implying zero value for the liquid mass fraction and the droplet number density at these boundaries. The 'outflow' condition is applied for these quantities at the ejector outlet. Here we would like to mention that the solvers diverge when the pressure values mentioned in 6.1 are abruptly applied at the motive and the suction inlets and at the outlet. We observe that the solvers converge perfectly when the boundary pressures are gradually changed to the final values over a small time duration (for a certain number of iterations for the steady solver) starting from a value equal to the average initial pressure in the domain. This is done with the B.4 B.5

6.1.1 Grid independence study

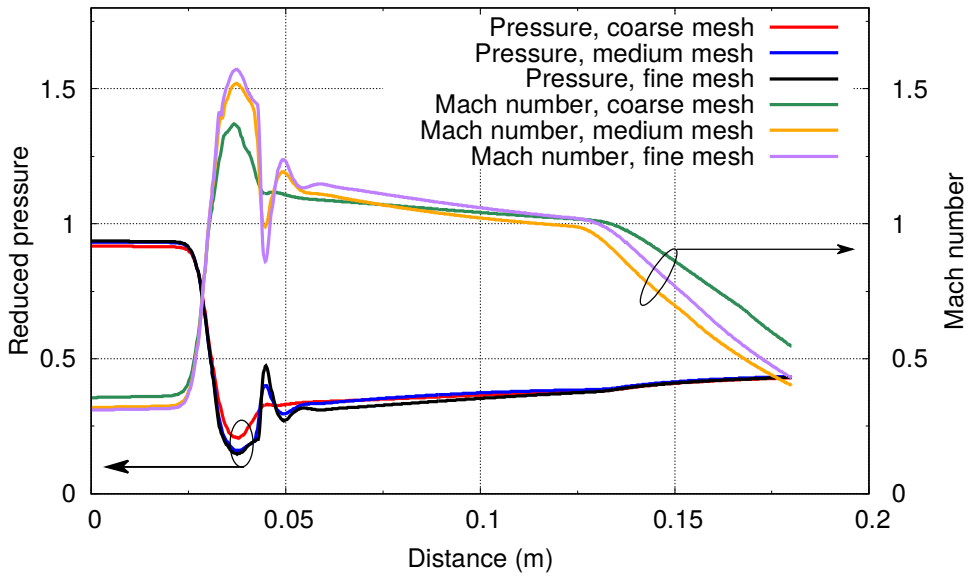

FIGURE 6.3: Distribution of the reduced pressure and Mach number along the ejector center line for three different meshes. The coarse mesh has 57056 hexahedral cells, the medium one has 678979 hexahedral cells while the fine mesh has 2118567 hexahedral cells.

Three different meshes, namely, the coarse mesh, the medium mesh and the fine mesh were tested in order to work with an optimum grid in terms of solution accuracy and required computational

effort. The coarse mesh has 57056 hexahedral cells, the medium one has 678979 hexahedral cells while the fine mesh has 2118567 hexahedral cells. For this grid independence study, only single phase simulations were performed on these meshes without any phase change occurring. The fine mesh takes too much time to converge on a 28 core machine with real gas properties of 6.3) shows the normalized pressure and Mach number distribution along the ejector center line for the three meshes. We observe that there is not much difference in the solution for pressure and Mach number calculated on the medium and the fine mesh. Therefore, we used the medium mesh with 678979 hexahedral cells for all the simulation data presented in this chapter. In the following section, we present and discuss the various results on the phase change process inside the ejector geometry.

6.2 Results and Discussions

Here we discuss the various results obtained by us based on the equilibrium and non-equilibrium compressible phase change solvers available in Ansys CFX. First we present the results based on the Redlich-Kwong equation of state already available in Ansys CFX and later we discuss the results based on the Span-Wagner equation of state from NIST Refprop.

6.2.1 Results based on the Redlich-Kwong equation of state

Here we present the results based on the Redlich-Kwong equation of state and the non-equilibrium solver. In the contour plots shown below, we show the distribution of two different physical quantities on mutually perpendicular planes one of which passes through the suction inlet.

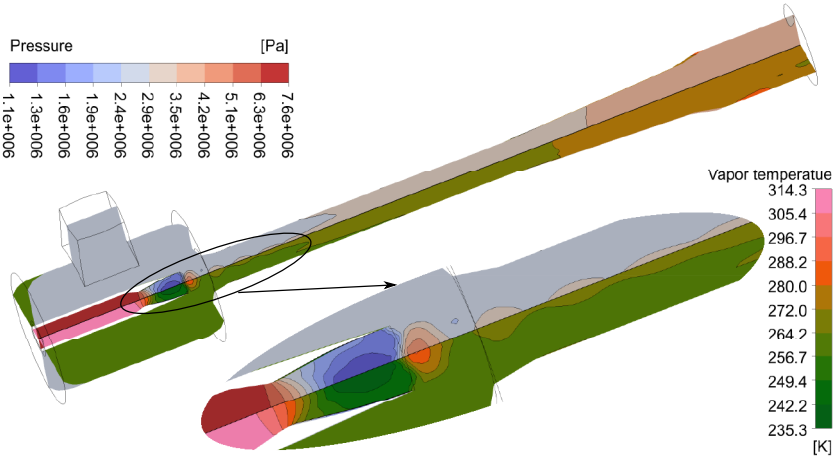

FIGURE 6.4: Pressure and temperature distribution inside the ejector calculated based on the Redlich-Kwong equation of state and the non-equilibrium solver. The zoomed view shows the distribution around the motive nozzle throat.

6.4) shows the distribution of pressure and temperature inside the ejector. We observe a minimum pressure of 11 bar and a minimum temperature of 235 K is predicted inside the motive nozzle diverging part.

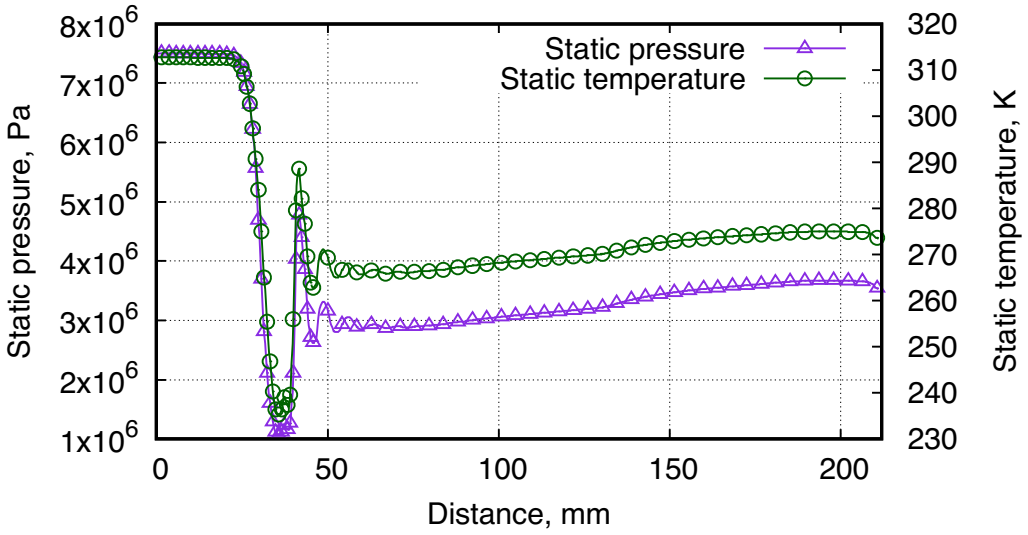

FIGURE 6.5: Pressure and temperature distribution along the ejector center line calculated based on the Redlich-Kwong equation of state and the non-equilibrium solver.

6.5) shows the temperature and pressure distribution along the ejector center line. It can be noticed that the non-equilibrium solver predicts a shock train outside the motive nozzle although it is not fully resolved by the solver.

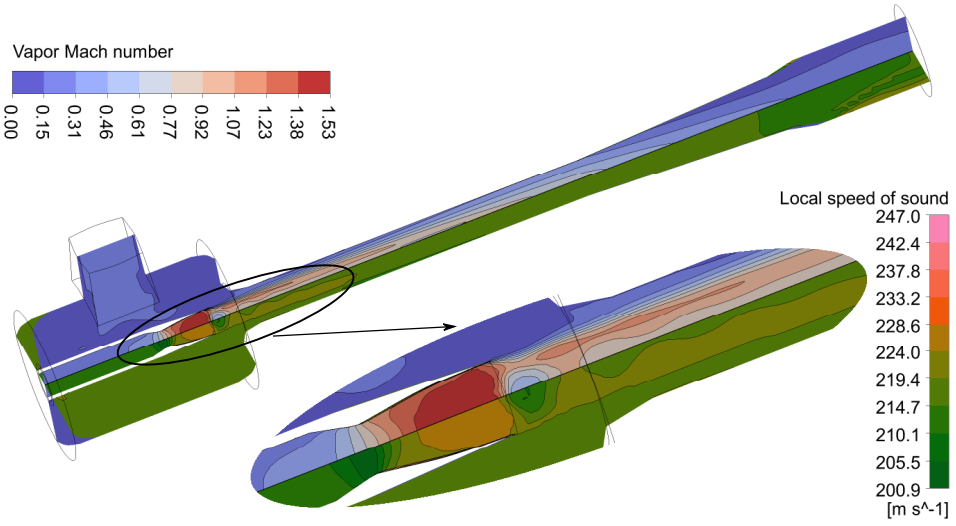

FIGURE 6.6: Mach number and local speed of sound distribution inside the ejector calculated based on the Redlich-Kwong equation of state and the non-equilibrium solver. The zoomed view shows the distribution around the motive nozzle throat.

6.6) shows the distribution of Mach number and local speed of sound inside the ejector. It can be seen that the Mach number is highest at the outlet of the motive nozzle where it is

abruptly reduced to subsonic values. The speed of sound is minimum at the throat of the motive nozzle and increases along the downstream till the shock at the nozzle outlet is encountered.

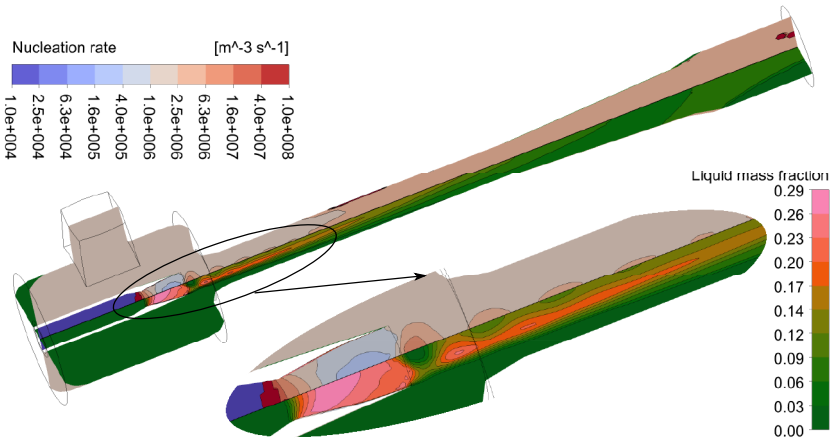

FIGURE 6.7: Nucleation rate and liquid mass fraction distribution inside the ejector calculated based on the Redlich-Kwong equation of state and the non-equilibrium solver. The zoomed view shows the distribution around the motive nozzle throat.

6.7) shows the distribution of nucleation rate and the liquid mass fraction inside the ejector. The nucleation starts before the motive nozzle throat wit a rate which is very high ($\sim 10^{33}$ nucleation per m^3 per second) and not shown in the figure for clarity. This rate reduces to $\sim 10^7$ nucleation per m^3 per second in a very short distance. Outside the motive nozzle, the nucleation rate is higher in the regions wherever the pressure is higher because of the oblique shock train. The maximum liquid mass fraction appears inside the motive nozzle and is equal to 0.29.

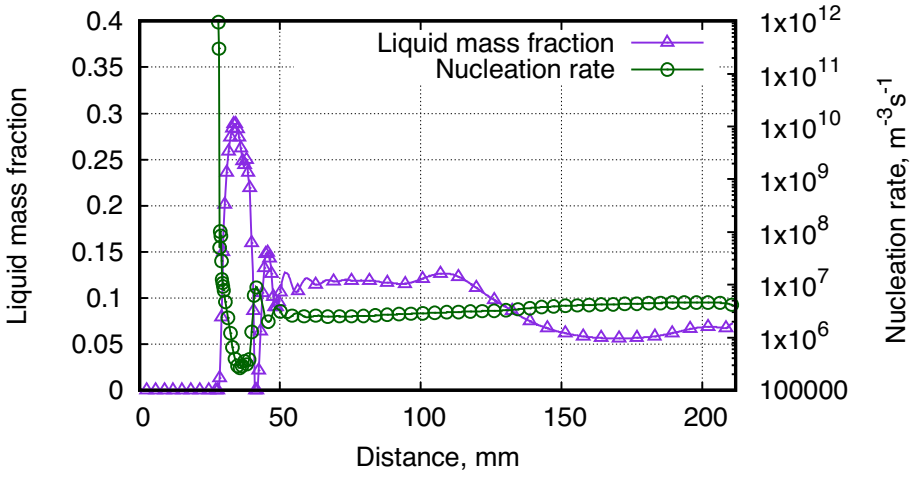

FIGURE 6.8: Nucleation rate and liquid mass fraction distribution along the ejector center line calculated based on the Redlich-Kwong equation of state and the non-equilibrium solver.

6.8) shows the distribution of nucleation rate and the liquid mass fraction along the ejector center line. It can be noticed that the liquid droplets evaporate completely because of

the heat generated by the shock outside the motive nozzle. A liquid fraction of 0.07 leaves the ejector outlet.

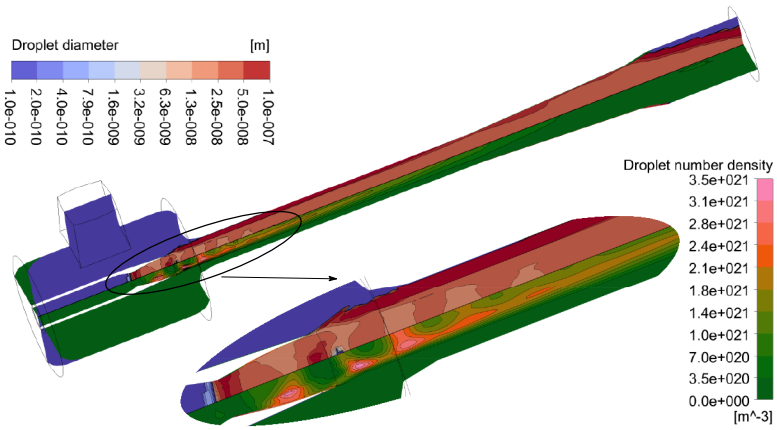

FIGURE 6.9: Droplet diameter and number distribution inside the ejector calculated based on the Redlich-Kwong equation of state and the non-equilibrium solver. The zoomed view shows the distribution around the motive nozzle throat.

6.9) shows the distribution of droplet diameter and droplet number density inside the ejector. The maximum droplet diameter predicted by the solver is around 0.1 μm and the maximum droplet number density is around 10^{21} droplets per m^3. The droplet size and number density distribution follow the distribution of pressure due to the oblique shock train.

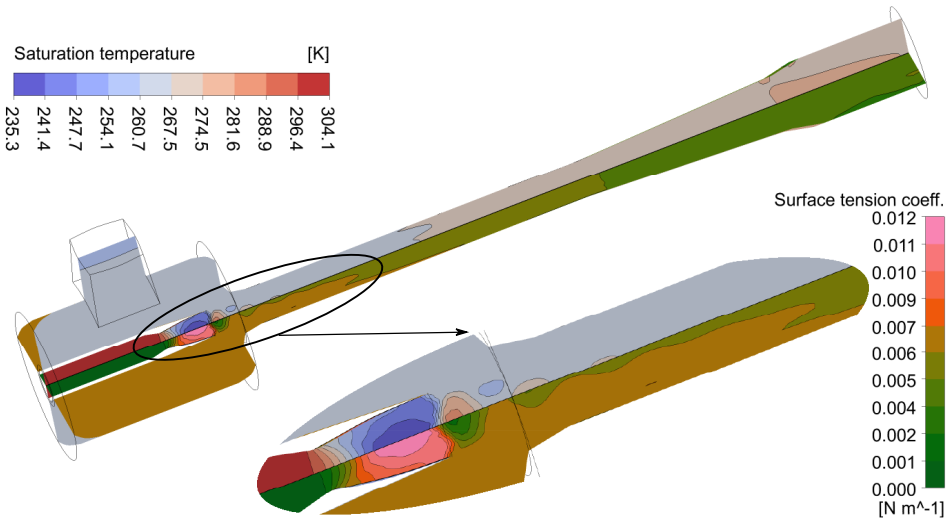

FIGURE 6.10: Saturation temperature and surface tension coefficient distribution inside the ejector calculated based on the Redlich-Kwong equation of state and the non-equilibrium solver. The zoomed view shows the distribution around the motive nozzle throat.

6.10) shows the distribution of saturation temperature and the surface tension coefficient inside the ejector. The saturation temperature is minimum ($\sim$ 235 K) and the surface tension coefficient is maximum ($\sim$ 0.012 N/m) inside the motive nozzle. The corresponding distribution

of saturation temperature and the surface tension coefficient along the ejector center line is 6.11).

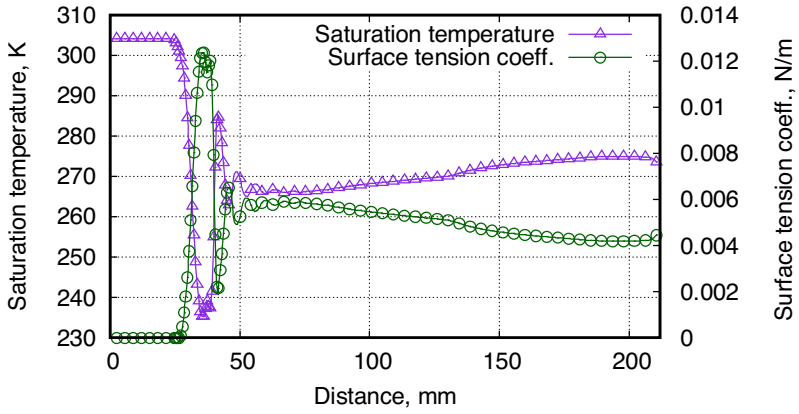

FIGURE 6.11: Saturation temperature and surface tension coefficient distribution along the ejector center line calculated based on the Redlich-Kwong equation of state and the non-equilibrium solver.

6.12) shows the distribution of turbulent kinetic energy and its dissipate rate inside the ejector. It can be noticed that both the kinetic energy as well as its dissipation are higher inside the shear layers present in the mixing region.

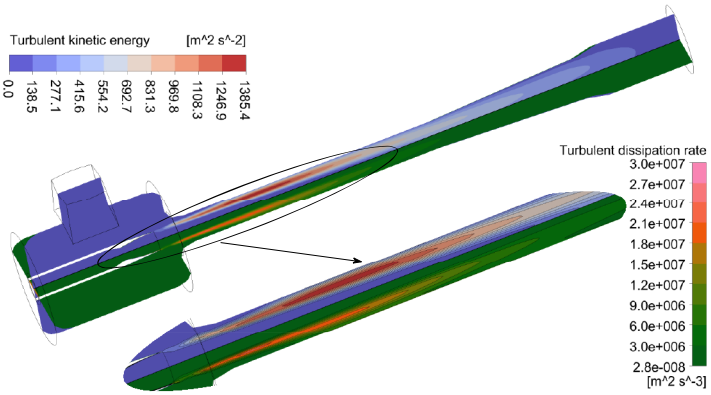

FIGURE 6.12: Turbulent kinetic energy and its dissipation distribution inside the ejector calculated based on the Redlich-Kwong equation of state and the non-equilibrium solver. The zoomed view shows the distribution around the motive nozzle throat.

6.2.2 Results based on Span and Wagner equation of state

In this section, we discuss the various results based on the Span-Wagner equation of state for R-744 which is not available in Ansys CFX. A FORTRAN based code is developed to extract the thermophysical data in tabular form which is then read in Ansys CFX. This is the most accurate equation of state for R-744 as concluded in the previous works on supercritical R-744

94 98]. We first present the results based on the equilibrium solver and later we present those based on the non-equilibrium solver.

6.2.2.1 Equilibrium solver based results

Here we discuss the results calculated based on the homogeneous equilibrium approach for the two phase flow of R-744 through the ejector geometry. The equilibrium phase change model assumes that the phase change occur at a much faster time scale compared to the fluid flow time scales. There is a mechanical, thermal and chemical potential equilibrium between the phases. The velocity, pressure, temperature and the Gibbs free enthalpy of the two phases are same in any grid cell containing the two phases. The two phases are treated as a fluid mixture with different thermophysical properties depending on the spatial distribution of the individual phases.

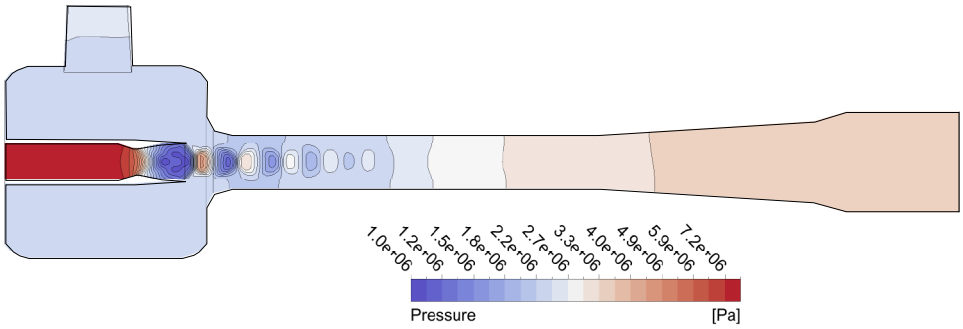

FIGURE 6.13: Pressure distribution inside the ejector based on equilibrium solver and thermophysical data of CO_2 from Span and Wagner equation of state.

6.13) shows the pressure distribution inside the ejector where we observe that the shock train is resolved much better by the equilibrium solver. The oblique shock train extends till the middle of the mixing section.

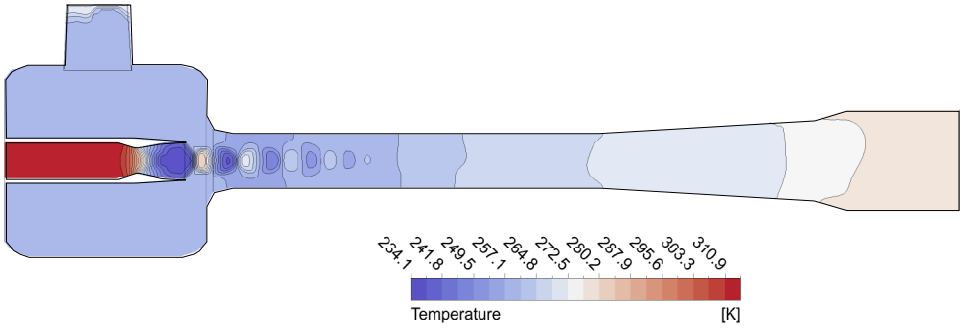

FIGURE 6.14: Temperature distribution inside the ejector based on equilibrium solver and thermophysical data of CO_2 from Span and Wagner equation of state.

6.14) shows the temperature distribution inside the ejector where again the better resolution of the shock train is evident. A minimum temperature of 234 K exists inside the motive nozzle while the temperature rises to 280 K for the fluid leaving the ejector outlet.

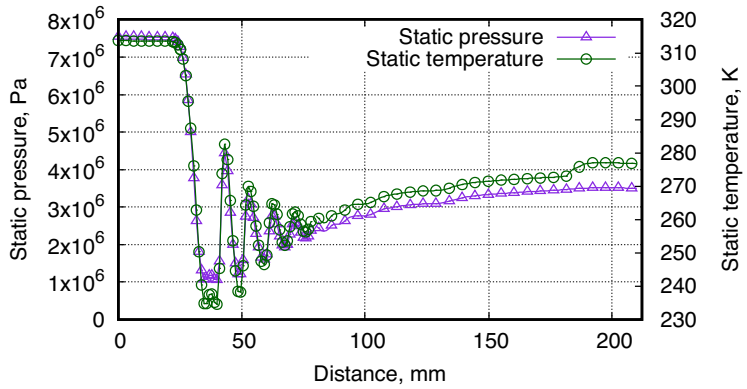

FIGURE 6.15: Pressure and temperature distribution along the ejector center line calculated based on the equilibrium solver.

The better resolution of the oblique shock train under the equilibrium solver can also be seen in 6.15) which shows the distribution of pressure and temperature along the ejector axis.

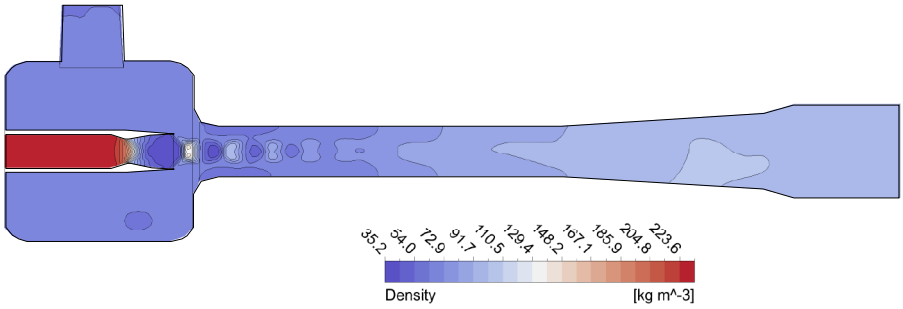

FIGURE 6.16: Density distribution inside the ejector based on equilibrium solver and thermophysical data of CO_2 from Span and Wagner equation of state.

6.16) shows the distribution of fluid density inside the ejector. A minimum density of around 35 kg/m^3 occurs inside the motive nozzle's diverging portion.

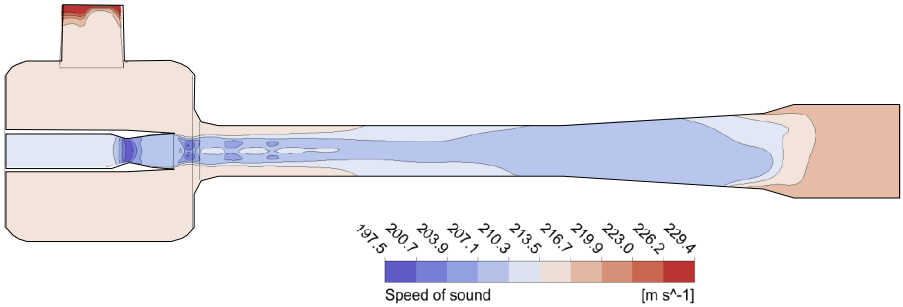

FIGURE 6.17: Speed of sound distribution inside the ejector based on equilibrium solver and thermophysical data of CO_2 from Span and Wagner equation of state.

6.17) shows the distribution of the local speed of sound inside the ejector. This speed is lowest at the throat of the motive nozzle and highest at the entry of the suction inlet.

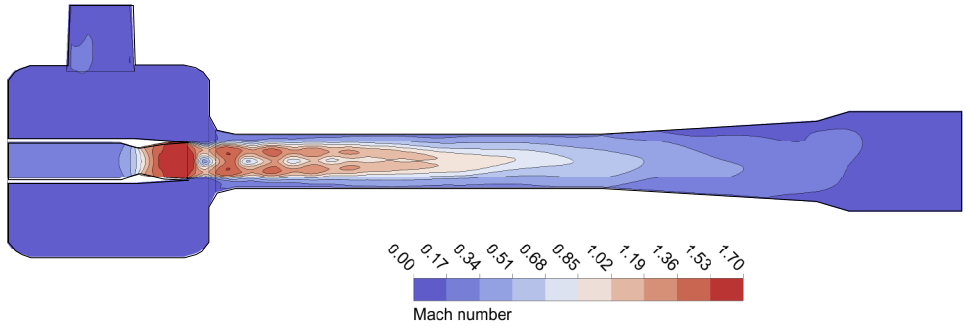

FIGURE 6.18: Mach number distribution inside the ejector based on equilibrium solver and thermophysical data of CO_2 from Span and Wagner equation of state.

6.18) shows the distribution of Mach number inside the ejector where one can notice that the maximum Mach number of 1.7 occurs at the outlet of the motive nozzle. The oblique shock train structure is much more clearly visible in this plot. The flow becomes subsonic as it leaves the ejector outlet with a Mach number of 0.17.

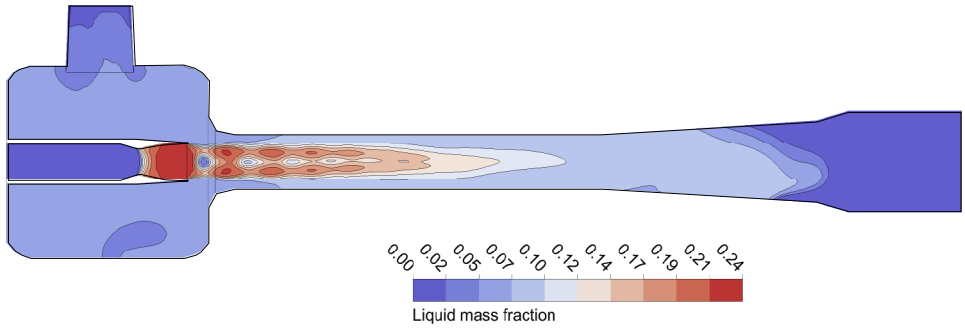

FIGURE 6.19: Liquid mass fraction distribution inside the ejector based on equilibrium solver and thermophysical data of CO_2 from Span and Wagner equation of state.

6.19) shows the distribution of liquid mass fraction inside the ejector. Again, the shock train structure is beautifully revealed with more liquid fraction present at low pressure locations and vice versa. A maximum liquid mass fraction of 0.24 is predicted by the solver inside the motive nozzle's diverging portion while the liquid is almost evaporated at the ejector's outlet.

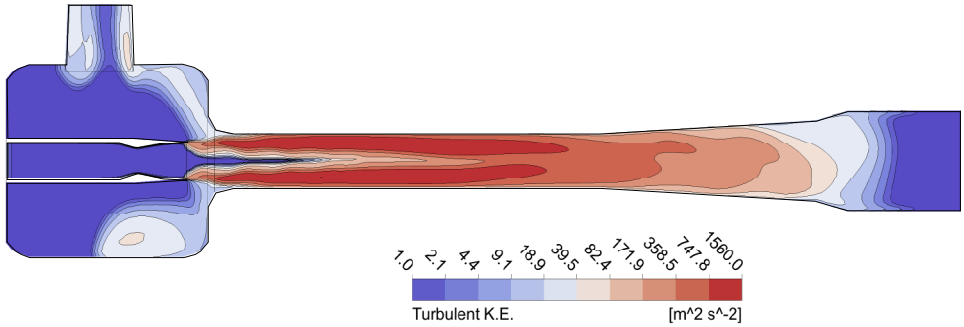

FIGURE 6.20: Turbulent kinetic energy distribution inside the ejector based on equilibrium solver and thermophysical data of CO_2 from Span and Wagner equation of state.

6.20 6.21) respectively show the distribution of turbulent kinetic energy and turbulent dissipation rate inside the ejector. The solver predicts similar distribution for these physical quantities with more kinetic energy and its dissipation rate inside the shear layers present in the mixing section.

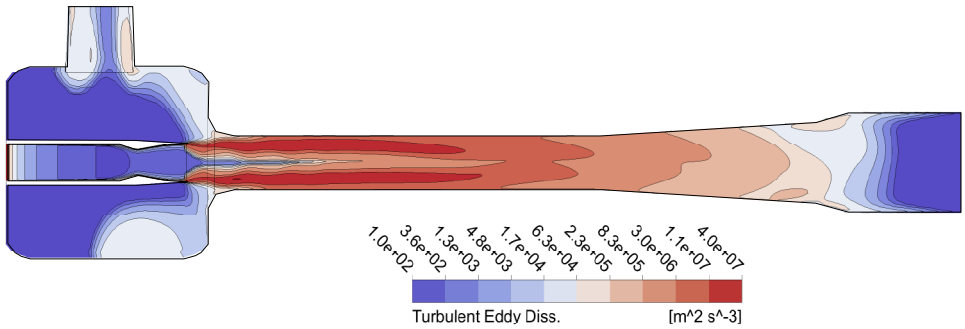

FIGURE 6.21: Turbulent energy dissipation distribution inside the ejector based on equilibrium solver and thermophysical data of CO_2 from Span and Wagner equation of state.

6.2.2.2 Non-equilibrium solver based results

The non-equilibrium phase change solver in Ansys CFX is based on the classical nucleation theory and it computes for the nucleation and growth of droplets in the rapidly expanding, supercooled fluid vapor. This model differs from the equilibrium phase change model as the two fluid phases can have different temperature and velocities under the non-equilibrium solver. The solver calculates the nucleation rate based on the Gibbs free enthalpy of the supercooled vapor, the surface tension coefficient between the two phases. It also calculates the droplet diameter and the droplet number density as the fluid moves through the ejector. In the figures shown below, we plot the distribution of various physical quantities on a plane passing through the ejector center line and normal to the suction inlet.

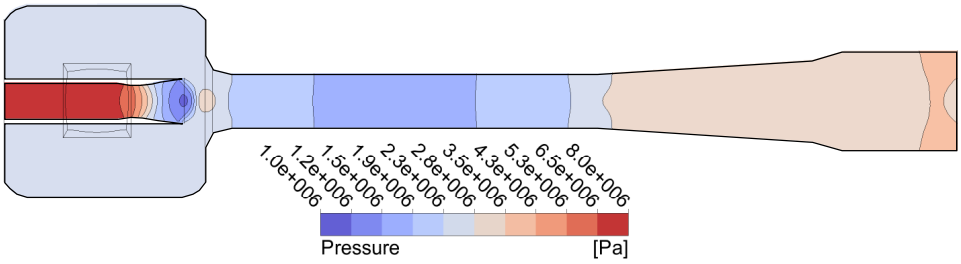

FIGURE 6.22: Pressure distribution inside the ejector based on non-equilibrium solver and thermophysical data of CO_2 from Refprop.

6.22) shows the pressure distribution predicted by the non-equilibrium solver inside the ejector. As can be seen, the oblique shock train structure is poorly resolved by the solver, only one oblique shock outside the motive nozzle is predicted by the solver. The minimum pressure in the motive nozzle and the pressure recovered in the diffuser section are similar to those predicted by the equilibrium solver.

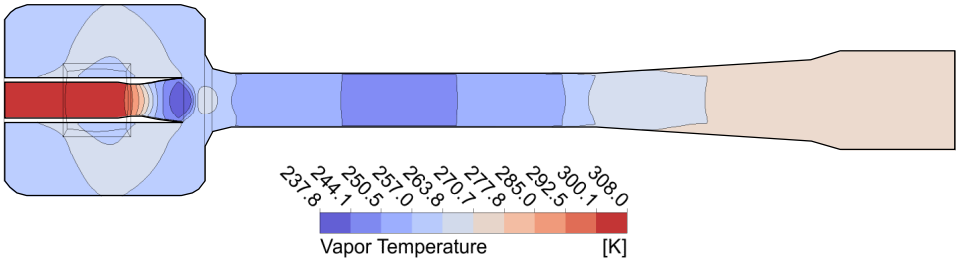

FIGURE 6.23: Vapor temperature distribution inside the ejector based on non-equilibrium solver and thermophysical data of CO_2 from Refprop.

The lack of resolution is also evident for the case of temperature of the vapor as can be seen in 6.23). A minimum temperature of 238 K is predicted by the solver in the motive nozzle while a temperature of 278 K is predicted at the ejector outlet.

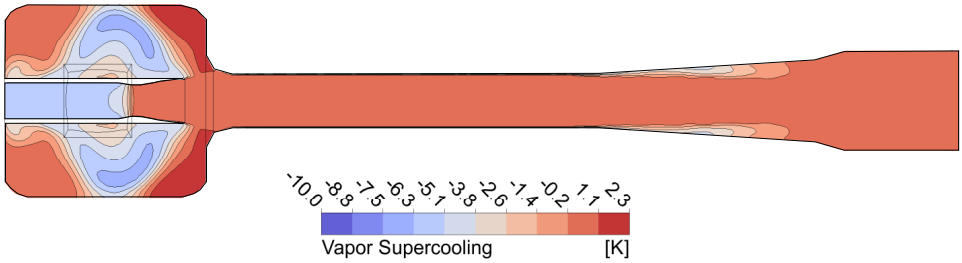

FIGURE 6.24: Vapor supercooling distribution inside the ejector based on non-equilibrium solver and thermophysical data of CO_2 from Refprop.

6.24) shows the supercooling attained by the vapor phase, the solver nonphysically predicts a supercooling of 1.1 K everywhere in the motive, mixing sections and most of the diffuser section. The magnitude of the supercooling appears to be correct as the spinodal limit

6.25)

shows the distribution of surface tension coefficient inside the ejector. The maximum surface tension (0.012 N/m) lies inside the motive nozzle's diverging portion while the ejector outlet has a much lower value of 0.005 N/m.

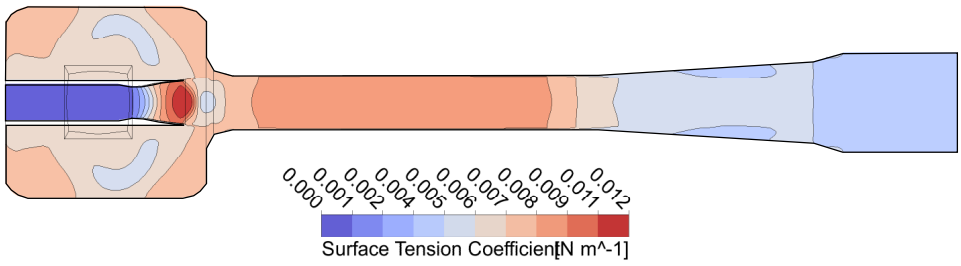

FIGURE 6.25: Surface tension coefficient distribution inside the ejector based on non-equilibrium solver and thermophysical data of CO_2 from Refprop.

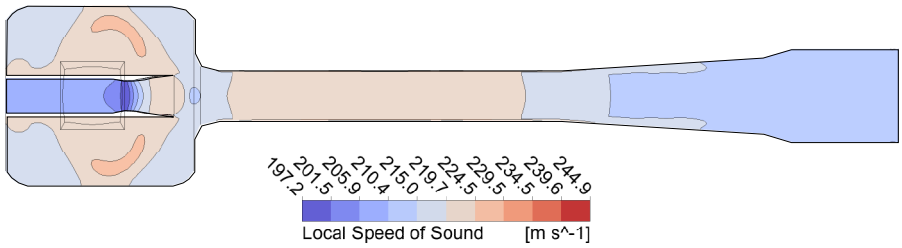

FIGURE 6.26: Speed of sound distribution inside the ejector based on non-equilibrium solver and thermophysical data of CO_2 from Refprop.

6.26 6.27) shows the Mach number inside the ejector as predicted by the non-equilibrium solver. As can be observed from the figures, the non-equilibrium solver predicts a single oblique shock outside the motive nozzle.

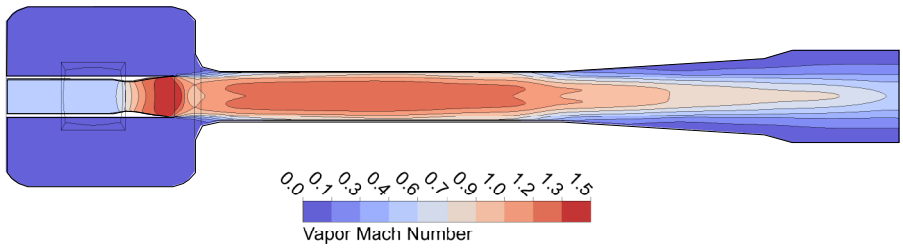

FIGURE 6.27: Mach number distribution inside the ejector based on non-equilibrium solver and thermophysical data of CO_2 from Refprop.

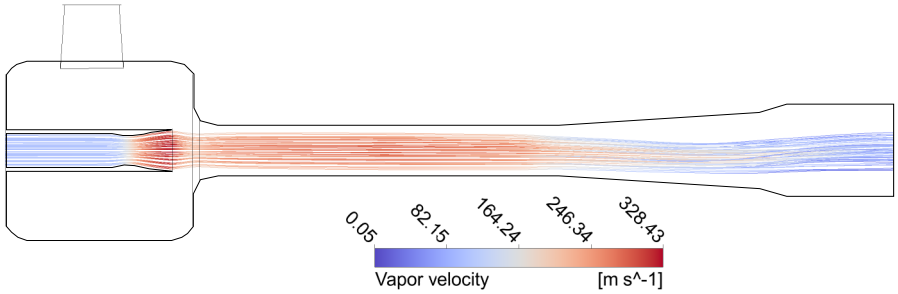

FIGURE 6.28: Streamlines from the motive nozzle colored by vapor velocity inside the ejector based on non-equilibrium solver and thermophysical data of CO_2 from Refprop.

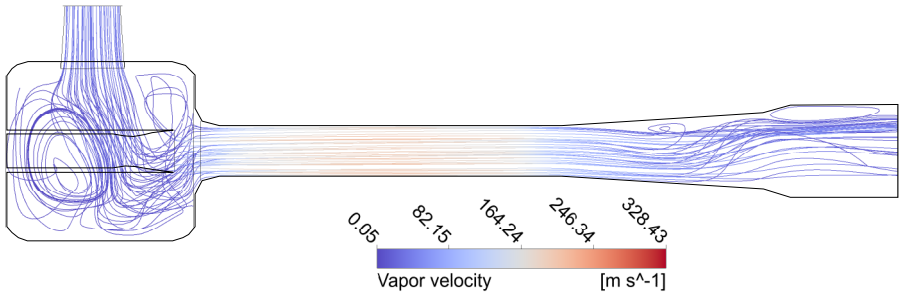

FIGURE 6.29: Streamlines from the suction nozzle colored by vapor velocity inside the ejector based on non-equilibrium solver and thermophysical data of CO_2 from Refprop.

6.28 6.29) show the distribution of streamlines inside the ejector which are colored by the vapor velocity and which originate from the motive and the suction nozzle respectively. It can be noticed that entrained fluid from the suction nozzle has lower velocity inside the ejector.

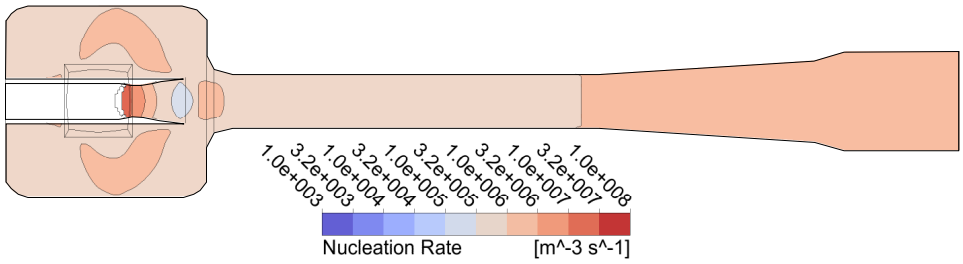

FIGURE 6.30: Nucleation rate distribution inside the ejector based on non-equilibrium solver and thermophysical data of CO_2 from Refprop. Very high rate ($\sim 10^{33}$ nucleation per m^3 per second) occurs at the start of converging portion of the motive nozzle.

6.30) shows the distribution of the nucleation rate inside the ejector. A maximum rate of $\sim 10^{23}$ nucleation per m^3 per second is predicted by the solver upstream of the motive nozzle's throat region. The nucleation rate decreases to $\sim 10^{8}$ nucleation per m^3 per second in a very short distance. A nucleation rate of $\sim 10^{7}$ nucleation per m^3 per second prevails inside the mixing section. A little higher nucleation rate is predicted by the solver inside the diffuser and the outlet sections.

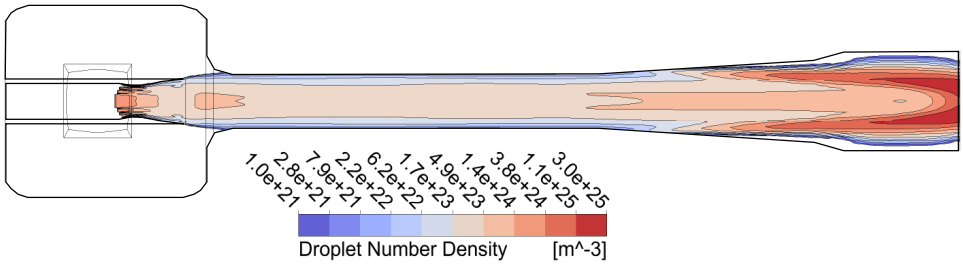

FIGURE 6.31: Droplet number density distribution inside the ejector based on non-equilibrium solver and thermophysical data of CO_2 from Refprop.

6.31) shows the droplet number density distribution inside the ejector where $\sim 10^{24}$ droplets per m^3 are present inside the motive, mixing, diffuser and the outlet sections.

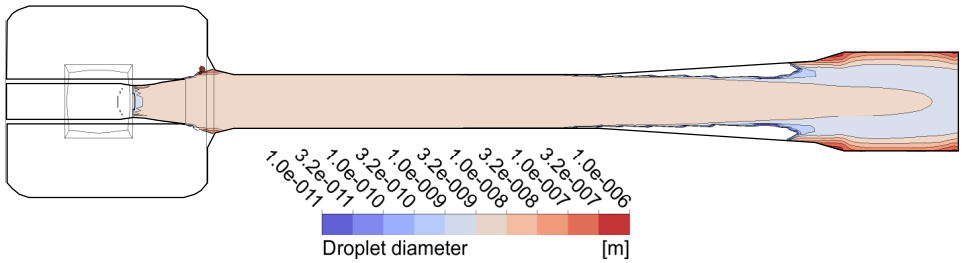

FIGURE 6.32: Droplet diameter distribution inside the ejector based on non-equilibrium solver and thermophysical data of CO_2 from Refprop.

6.32) shows the distribution of droplet diameter inside the ejector. It can be observed that the motive nozzle, the mixing section and most of the diffuser section have droplets of size equal to 10^{-8} m.

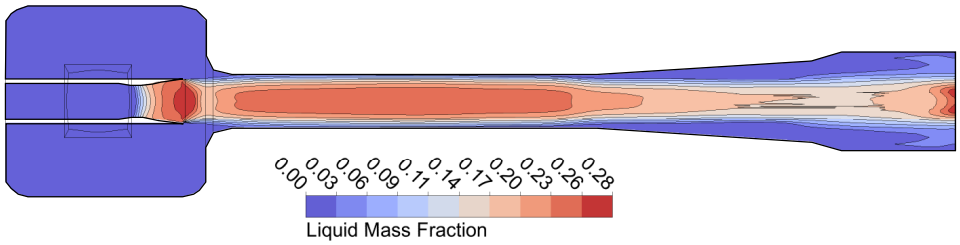

FIGURE 6.33: Liquid mass fraction distribution inside the ejector based on non-equilibrium solver and thermophysical data of CO_2 from Refprop.

6.33) shows the distribution of liquid mass fraction inside the ejector. The solver predicts a maximum liquid mass fraction of 0.28 at the outlet of the motive nozzle while it is equal to 0.26 inside most of mixing section.

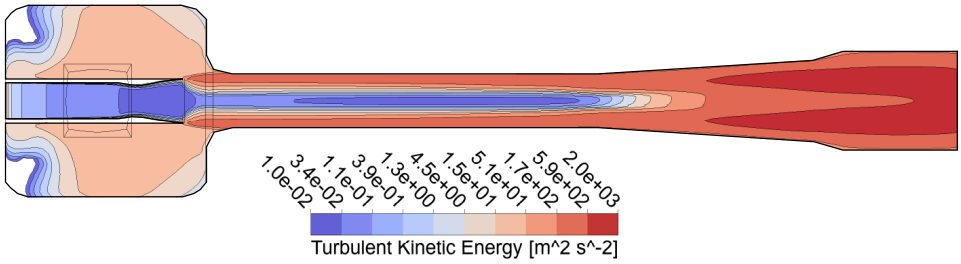

FIGURE 6.34: Turbulent kinetic energy distribution inside the ejector based on non-equilibrium solver and thermophysical data of CO_2 from Refprop.

6.34 6.35) respectively show the distribution of turbulent kinetic energy and its dissipation rate inside the ejector. The non-equilibrium solver predicts a very low kinetic energy and low dissipation rate in the axial region of the mixing section. Both of these quantities are higher inside the annular region in the mixing section indicating a higher turbulence in the region where the motive and section streams are mixing. The magnitude of these quantities are also higher in the diffuser and the outlet sections of the ejector.

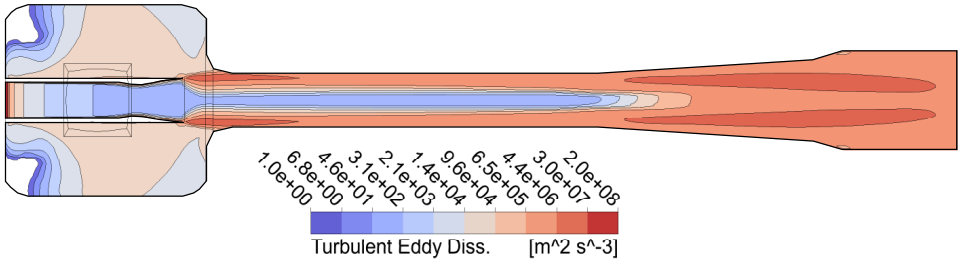

FIGURE 6.35: Turbulent energy dissipation distribution inside the ejector based on non-equilibrium solver and thermophysical data of CO_2 from Refprop.

6.3 Summary

Here we summarize the work performed on the phase change process of R-744 inside the ejector geometry. The summary is given in the form of following points:

- The equilibrium and the non-equilibrium solvers predict different flow structure outside the motive nozzle. The equilibrium solver predicts an oblique shock train while the non-equilibrium solver predicts a single shock outside the motive nozzle.
- With respect to the phase change process, the motive nozzle plays a central role. Lowest amount of pressure, temperature and the highest amount of Mach number, surface tension and the liquid mass fraction occur inside the motive nozzle. Noticeable amount of the liquid phase first appears after the throat of the motive nozzle and then the amount of liquid increases along the downstream in the diverging portion of the nozzle. The liquid

fraction is affected by the shock structure outside the nozzle but is advected by the flow throughout the mixing section and even through the diffuser section.

- The nucleation of the liquid droplets starts with a very high rate ($\sim 10^{33}$ nucleation per m^3 per second) upstream of the motive throat and then decreases rapidly ($\sim 10^{8}$ nucleation per m^3 per second) after the throat. A droplet number density of $\sim 10^{23}$ droplets per m^3 and a droplet radius of $\sim 10^{-8}$ prevails in most of the motive nozzle, the mixing section, and the diffuser section. Both the equilibrium and the non-equilibrium solvers predict almost similar value of the maximum liquid mass fraction distribution outside the motive nozzle.

- Ansys CFX predicts a vapor supercooling of around 1.1 inside most of the ejector. The magnitude seems to be physically correct based on the inlet state of 80 bar, 315 K. The spinodal limit itself is near to the saturated vapor line for this motive inlet state. However, the supercooling is expected to be very low once the phase change process has initiated.

- There is a higher value of turbulent kinetic energy predicted inside an annular region in the mixing section, particularly near the mixing inlet. Similarly, the magnitude of the dissipation rate is also higher in the same region. This indicates the presence of higher turbulence in the shear layers causing fluid mixing inside the mixing region.